AIP | Physics of Fluids

Fluid-structure interaction in deformable microchannels

Debadi Chakraborty, J. Ravi Prakash, James Friend, and Leslie Yeo

Citation: Phys. Fluids **24**, 102002 (2012); doi: 10.1063/1.4759493
View online: http://dx.doi.org/10.1063/1.4759493
View Table of Contents: http://pof.aip.org/resource/1/PHFLE6/v24/i10
Published by the American Institute of Physics.

Fluid-structure interaction in deformable microchannels

Debadi Chakraborty,[1,a)] J. Ravi Prakash,[1] James Friend,[2,3] and Leslie Yeo[2,b)]
[1]*Department of Chemical Engineering, Monash University, Melbourne, Victoria 3800, Australia*
[2]*Micro/Nanophysics Research Laboratory, School of Electrical and Computer Engineering, RMIT University, Melbourne, Victoria 3000, Australia*
[3]*Melbourne Centre for Nanofabrication, Clayton, Victoria 3800, Australia*

(Received 27 March 2012; accepted 3 October 2012; published online 19 October 2012)

A polydimethylsiloxane microfluidic device composed of a single microchannel with a thin flexible layer present over a short length along one side of the channel was fabricated and modelled in order to investigate the complex fluid-structure interaction that arises between a flowing fluid and a deformable wall. Experimental measurements of thin layer deformation and pressure drop are compared with predictions of two- and three-dimensional computational models that numerically solve the coupled set of equations governing both the elasticity of the thin layer and the fluid. It is shown that the two-dimensional model, which assumes the flexible thin layer comprises an infinitely wide elastic beam of finite thickness, reasonably approximates a three-dimensional model, and is in excellent agreement with experimental observations of the thin layer profile when the width of the thin layer is beyond a critical value, roughly twice the length of the thin layer. © *2012 American Institute of Physics*. [http://dx.doi.org/10.1063/1.4759493]

I. INTRODUCTION

The fabrication of microfluidic devices from soft polymers or elastomers has gained considerable interest in the last decade. The attractiveness of these soft materials stems from the ability to specifically tailor their physicochemical properties to a particular application, the lower material and fabrication costs which allows the possibility for disposable devices, and the impressive durability of polymer-based materials compared to conventional materials used in microfabrication, such as silicon and glass.[1] Moreover, soft polymers like polydimethysiloxane (PDMS)[2] offer excellent optical transparency, gas permeability, and biocompatibility, all vital to on-chip cell culturing, constituting the fabrication material of choice for a large proportion of microfluidic devices for cellomics, drug screening, and tissue engineering.[3]

The bonding strength, ability to mould (even at the nanoscale), biocompatibility, transparency, and flexibility of these elastomeric substrates also make them ideal for fabricating microfluidic actuation structures. For example, thin PDMS layers have been employed as diaphragms or interfaces for pneumatic actuation and control in microchannels,[4–7] as well as substrates for biological characterisation and manipulation in microdevices.[8–10] More sophisticated microfluidic actuation structures have also been proposed, including multilayer and branched channel networks controlled by elastomeric micropumps and microvalves[11] for a variety of uses, including spatiotemporal control of chemical gradients for chemotaxis studies on a microfluidic chip.[12]

Fundamental studies to investigate the complex fluid-structural interaction arising from these flexible materials and the flow of the fluid within them, however, have not matched the rapid pace of developments in applications using these materials. In fact, there have been no studies undertaken

[a)]Current address: Department of Mathematics and Statistics, The University of Melbourne, Victoria 3010, Australia.
[b)]To whom correspondence may be addressed. Email: leslie.yeo@rmit.edu.au.

to investigate the flow through flexible channels at scales commensurate with microfluidic devices. Even simple experiments[13–22] and theoretical studies[23–28] undertaken to investigate Newtonian flows through *macroscopic* deformable tubes have yet to be reproduced at the *microscale*, where channel dimensions are on the order of 10–100 μm and the Reynolds number Re is typically of the order of unity or below, typically two or more orders of magnitude smaller than the $\mathcal{O}(10^4\ \mu\text{m})$ channel dimensions and $\mathcal{O}(100)$ or greater Reynolds numbers examined in these studies. Moreover, there is no evidence in the literature of the use of a fluid-structural interaction theory to model a collapsible microchannel to the best of our knowledge, despite the presence of such structures in nature—particularly in vascular flow—and the potential usefulness of collapsible channels for valving and similar applications. Given that the flow of a fluid within a flexible structure is regulated by the stresses imposed upon the structure by both the fluid and any external forces, the rheological properties of the fluid and the mechanical properties of the structure together significantly influence the flow in the system. In particular, the stresses exerted by the fluid on the flexible wall cause its deformation, consequently altering the fluid flow characteristics and therefore the stresses themselves, intricately coupling the fluid and surrounding structure in a manner that requires the modelling and solution of the moving fluid-solid boundary. In order to understand microscale fluid-structural interaction phenomena, an adequate theory, validated by experimental data, is therefore necessary.

Given this motivation, we carried out a fundamental investigation of the fluid flow past a deformable *microchannel*. Using a custom fabricated microfluidics device that houses a flow-through microchannel with a small deformable region that is controlled through externally applied air pressure, we compared displacement profiles of the small deformable region measured experimentally with that predicted using a two- and three-dimensional finite element model that incorporates coupling between the thin wall and the fluid in the flow-through microchannel. We fabricated the 200 μm high, 29×10^3 μm long flow-through microchannel structure in PDMS, introducing a pressure microchamber in the PDMS structure adjacent to the flow-through microchannel. The PDMS layer present between the microchamber and microchannel forms the small deformable region—the thin wall that interacts with the fluid in the flow-through microchannel.

The rest of the article is organised as follows. We first formulate the numerical model and discuss the solution methodology in Sec. II. The fabrication and design of the deformable microchannel and the experimental methodology is subsequently described in Sec. III. A comparison between the results obtained from both the experiments and numerical simulation then follows in Sec. IV, after which we summarise our conclusions in Sec. V.

II. NUMERICAL SIMULATION AND SOLUTION METHODOLOGY

A. Two-dimensional finite element model for fluid-structure interaction (2D-FEM-FSI)

To match the geometry of the flow-through microchannel and the thin flexible wall along a short portion of its side *width* in the experimental design (discussed subsequently in Sec. III) and shown in Fig. 1, we consider a two-dimensional model of the experimental setup illustrated in Fig. 2(a) in which fluid flows through a section of the microchannel with height H, along a side of which a short segment of elastic thin layer BC with thickness t and length L spanning the entire channel *width* exists. While the sidewalls of the channel adjacent to the thin layer section, AB and CD with lengths L_u and L_d, respectively, are considered rigid, the thin layer is allowed to deform under an external pressure p_e as measured in the air pressure chamber. To mimic the experimental geometry, we set $H = 200\,\mu$m, $L_u = 14 \times 10^3$ μm, $L = 1 \times 10^3$ μm, $L_d = 14 \times 10^3$ μm, and $t = 60\,\mu$m. Here, the x-axis spans the channel length whereas the z-axis denotes the height of the channel with origin at point O.

In the absence of body forces, negligible considering the microscopic scale, the equations of motion for steady, incompressible flow are governed by conservation of mass and momentum,

$$\nabla \cdot \boldsymbol{v} = 0, \tag{1}$$

$$\rho\, \boldsymbol{v} \cdot \nabla \boldsymbol{v} = \nabla \cdot (-p\, \mathbf{I} + \boldsymbol{\tau}), \tag{2}$$

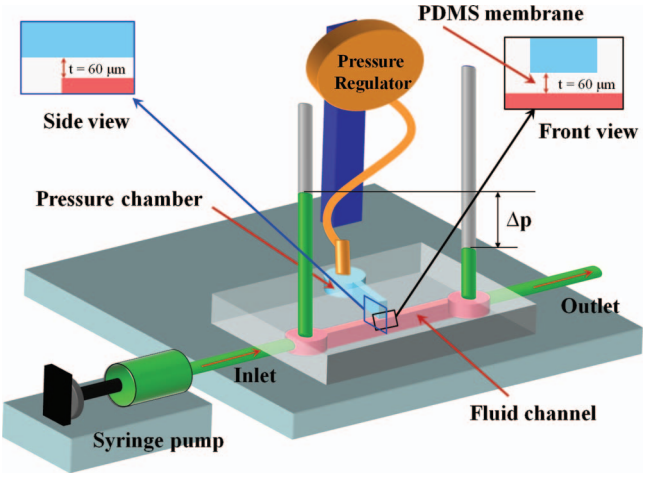

FIG. 1. Illustration of the experimental setup, indicating the inlet and outlet ports, methods of flow control and pressure measurement, and the short region over which the channel is deformed using an external pressure applied tangent to the main fluid channel.

respectively, where ρ is the fluid density, $\boldsymbol{v}$ its velocity field, p its pressure, and $\boldsymbol{\tau}$ is the viscous stress tensor; $\mathbf{I}$ represents the identity tensor. For a Newtonian fluid, $\boldsymbol{\tau} = 2\eta\mathbf{D}$, where η is the fluid viscosity and $\mathbf{D} = \frac{1}{2}(\nabla\boldsymbol{v} + \nabla\boldsymbol{v}^{\mathrm{T}})$ is the strain rate tensor.

Given the deformability of the thin layer under external pressure, the system comprises a moving-boundary problem in which the fluid flow and the solid domain that constitutes the thin elastic boundary film are coupled. As we are only interested in steady flow, the inertia of the solid

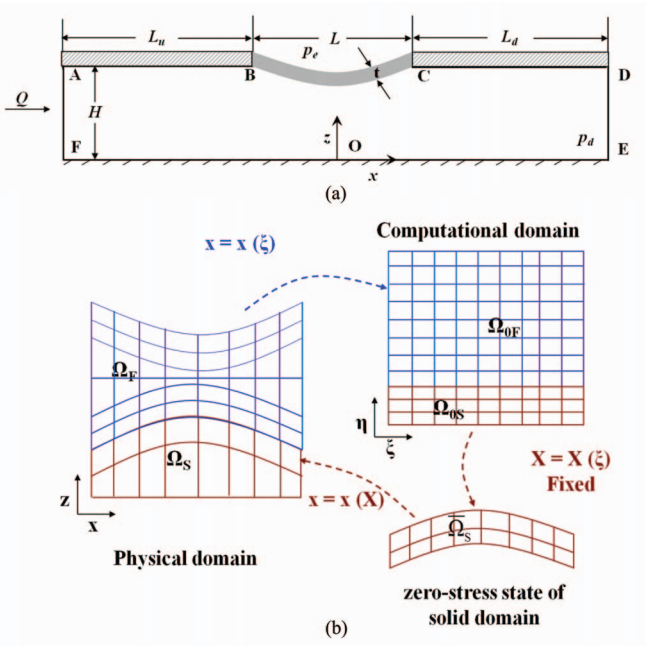

FIG. 2. (a) Geometry of the two-dimensional deformable microchannel defining the solution space for the numerical simulation. (b) The solution strategy for the moving-boundary coupling between the fluid and solid domains is handled by mapping the physical fluid domain to a reference computational domain ($\Omega_F \rightarrow \Omega_{0F}$) and the physical solid domain to a reference zero-stress domain($\Omega_S \rightarrow \overline{\Omega}_S$). We note that the solution of the elasticity equations itself constitutes a mapping from the zero-stress configuration ($\overline{\Omega}_S \rightarrow \Omega_S$), and consequently these equations are not solved separately. The mapping from the computational domain (Ω_{0S}) to the zero-stress configuration ($\overline{\Omega}_S$) is fully defined and known, requiring only a change of the domain of integration.

component does not affect the overall dynamics of the system. We therefore employ a solution strategy that continuously maps the fluid and solid domains $\boldsymbol{x} = \boldsymbol{x}(\boldsymbol{\xi})$, both unknown *a priori*, to arbitrary reference domains following the approach of Carvalho and Scriven,[29] as illustrated in Fig. 2(b). Here, the physical and reference computational domains are parameterised by the position vector $\boldsymbol{x}$ and $\boldsymbol{\xi}$, respectively, and $\boldsymbol{X}$ represents the position in the reference stress-free domain. The physical fluid domain Ω_F is mapped by elliptic mesh generation to a reference computational domain Ω_{0F}, where Eqs. (1) and (2) are solved. Due to the complexity in the geometry, the physical domain cannot be mapped to a simpler, quadrangular reference domain. Instead, it is more convenient to subdivide the physical domain into subdomains, then map those subdomains individually into separate subdomains that, together, comprise the reference computational domain. Here we use a boundary-fitted, finite element-based elliptic mesh generation method[30–33] that involves solving the following elliptic differential equation for the mapping:

$$\nabla \cdot \tilde{\mathbf{D}} \cdot \nabla \boldsymbol{\xi} = 0, \tag{3}$$

where the dyad $\tilde{\mathbf{D}}$ is a function of $\boldsymbol{\xi}$ in a manner analogous to a diffusion coefficient, that controls the spacing of the coordinate lines.[32]

The physically deformed solid domain constituting the thin flexible layer Ω_S, on the other hand, is mapped to a reference domain that, for convenience, we choose as a hypothetical zero-stress state where the stress tensor vanishes over the entire thin layer (which may not and need not be physically realisable). It is in this stress-free domain $\overline{\Omega}_S$ where the elasticity equations governing the deformation of the thin solid layer are solved, although the solution of these equations itself constitutes a mapping from the zero-stress configuration $\overline{\Omega}_S$ to the deformed domain Ω_S. The mapping from the computational domain Ω_{0S} to the zero-stress configuration $\overline{\Omega}_S$ is known and only requires a change of the domain of integration.

In the reference stress-free domain $\overline{\Omega}_S$, the equilibrium equation that governs the solid if acceleration and body forces may be neglected, reads

$$\nabla_X \cdot \mathbf{S} = 0, \tag{4}$$

where $\nabla_X = \sum_{j=1}^{3} \hat{\mathbf{E}}_j \partial / \partial X_j$, $\hat{\mathbf{E}}_j$ is the unit vector in the zero-stress state, and $\mathbf{S}$ is the first Piola-Kirchhoff stress tensor. We note that this is related to the original deformed state of the solid, i.e., the physical solid domain, through Piola's transformation to the Cauchy stress tensor $\boldsymbol{\sigma}$ by

$$\mathbf{S} = \mathbf{F}^{-1} \cdot \boldsymbol{\sigma}, \tag{5}$$

where

$$\mathbf{F} = \frac{\partial \boldsymbol{x}}{\partial \boldsymbol{X}} \tag{6}$$

is the deformation gradient tensor, which relates the undeformed state $\boldsymbol{X} = (X, Y, Z)$ to the deformed state $\boldsymbol{x} = (x, y, z)$. Closure is obtained through a constitutive relationship that relates the Cauchy stress tensor with the strain. For a neo-Hookean material, this takes the form

$$\boldsymbol{\sigma} = -\pi^* \mathbf{I} + G\mathbf{B}, \tag{7}$$

where $\pi*$ is a hydrostatic pressure-like scalar function, G is the shear modulus and $\mathbf{B} = \mathbf{F} \cdot \mathbf{F}^T$ is the left Cauchy-Green deformation tensor.

The equations governing the fluid motion and the solid deformation are subject to the following boundary conditions:

1. No-slip boundary conditions apply on the rigid walls, i.e., $\boldsymbol{v} = \mathbf{0}$ on $-(L_u + L/2) \le x \le (L_d + L/2)$ when $z = 0$ and $-(L_u + L/2) \le x \le -L/2$ and $L/2 \le x \le (L_d + L/2)$ when $z = H$.
2. Zero displacement is prescribed along both the left and right sides of the solid, i.e., $\boldsymbol{x} = \boldsymbol{X}$ on $H \le z \le H + t$ when $x = \pm L/2$.
3. At the upstream boundary ($0 \le z \le H$, $x = -(L_u + L/2)$), a fully developed velocity profile is specified, i.e., $v_z = 0$ and $v_x = f(z/H) = 6\,U_0\,(z/H)\,[1 - (z/H)]$, where U_0 is the average inlet velocity.
4. At the downstream boundary ($0 \le z \le H$, $x = (L_d + L/2)$), a fully developed flow boundary condition is imposed, i.e., $\mathbf{n} \cdot \nabla \boldsymbol{v} = \mathbf{0}$.

5. A force balance and a no-penetration condition is prescribed at the interface between the liquid and solid domain:

$$\mathbf{n} \cdot \boldsymbol{\tau} = \mathbf{n} \cdot \boldsymbol{\sigma} \quad \text{and} \quad \boldsymbol{u} = \boldsymbol{v}, \tag{8}$$

where $\boldsymbol{u}$ is the velocity of the solid and $\mathbf{n}$ is the outward unit vector normal to the deformed solid surface.

6. A force balance is prescribed at the top surface:

$$\mathbf{n} \cdot \boldsymbol{\sigma} = -p_e \mathbf{n}. \tag{9}$$

7. We have compared our theory with only the pressure drop in the experiments, and hence the gauge pressure of the fluid at the downstream boundary is defined as the datum *zero* pressure, i.e., $p_d = 0$.

The weighted residual form of Eqs. (1)–(4), obtained by multiplying the governing equations with appropriate weighting functions and subsequently integrating over the current domain, results in a large set of coupled nonlinear algebraic equations, solved subject to the specified boundary conditions using Newton's method with an analytical Jacobian, frontal solver, and first-order arclength continuation in parameters.[33–36] The formulation of the fluid-structure interaction problem posed here follows the procedure introduced by Carvalho and Scriven[29] in their examination of roll cover deformation in coating flows. *It turns out, however, that the weighted residual form of Eq.* (4) *used in their finite element formulation is incorrect.* While insignificant for small deformations, this error leads to significant discrepancies when the deformation is large. The weighted-residual equation is corrected here and validated in Appendix A against predictions using commercial finite element software ANSYS 11.0[37] for the deformation of a simple beam of neo-Hookean material fixed at its edges that we describe next.

B. ANSYS finite element model (2D/3D-ANSYS)

We expect our two-dimensional numerical simulation to reasonably approximate a three-dimensional system when the microchannel and hence thin film width is large compared to the height and length of the microchannel, such that boundary effects at the edges of the thin film are negligible. To determine the limits of the microchannel width at which the two-dimensional approximation breaks down, we carried out a three-dimensional finite element simulation involving a plane-strain model for a compressible neo-Hookean solid, since the incompressible neo-Hookean model described in Sec. II A has been developed for a two-dimensional geometry. For a given strain energy density function or elastic potential function of a neo-Hookean material,

$$\widehat{W} = \frac{G}{2}(I_1 - 3) + \frac{1}{d}(J-1)^2, \tag{10}$$

where $I_1 = \text{tr}(\mathbf{C})$ is the first invariant of the right Cauchy-Green deformation tensor $\mathbf{C} = \mathbf{F}^T \cdot \mathbf{F}$, G is the initial shear modulus of the material, d is the material incompressibility parameter, and $J = \det(\mathbf{F})$ is the ratio of the deformed elastic volume over the undeformed volume of material, the corresponding stress component is

$$\widehat{\mathbf{S}} = 2\frac{\partial \widehat{W}}{\partial \mathbf{C}}, \tag{11}$$

where $\widehat{\mathbf{S}}$ is the second Piola-Kirchoff stress tensor. If acceleration and body forces are negligible, the equilibrium equation for the deformed configuration is then

$$\nabla_x \cdot \boldsymbol{\sigma} = 0, \tag{12}$$

in which the Cauchy stress tensor is related to the second Piola-Kirchoff stress tensor in Eq. (11) by $\boldsymbol{\sigma} = J^{-1}\mathbf{F} \cdot \widehat{\mathbf{S}} \cdot \mathbf{F}^T$. Here ∇_x is defined by $\sum_{j=1}^{3} \hat{\mathbf{e}}_j \partial/\partial x_j$, where $\hat{\mathbf{e}}_j$ is the unit vector in the deformed state.

The equations governing the solid deformation above are subject to the following boundary conditions:

1. Zero displacement is prescribed along all side edges of the solid.
2. A force balance is prescribed at the top surface:

$$\boldsymbol{n} \cdot \boldsymbol{\sigma} = -p_e \boldsymbol{n}. \tag{13}$$

3. The pressure at the bottom surface is set to the datum value of zero.

The weighted-residual forms of the equilibrium equation (Eq. (12)) and the boundary conditions are solved in ANSYS 11.0[37] by using a Galerkin finite element method combined with a Newton-Raphson iteration scheme. In the solid domain, 8-node hexahedral elements (SOLID185) and 4-node elements (PLANE182) are used for the 3D and 2D simulations, respectively. To simulate the geometry described, we have used 105 elements for the 2D model, while for the 3D model, the number of elements are varied from 1050 to 10 500 depending on the width of the thin layer.

The simulations were carried out for the thin layer geometry shown in Fig. 3(a) in the absence of fluid to compare the predictions in the thin layer deformation under an externally applied pressure between the two- and three-dimensional models. Through initial simulations of the full geometry mimicking the experimental setup, including the microchannel and pressure chamber, we verified the deformation was insensitive to the physical presence of the pressure chamber and the microchannel, at least when the fluid is absent. Hence, it was sufficient to simulate a rectangular thin layer of thickness 60 μm and length 1×10^3 μm with fixed edges. The effect of varying the thin layer width (0.2×10^3, 0.5×10^3, 1.0×10^3, 2.0×10^3, 3.0×10^3, and 4.0×10^3 μm) was examined and compared to a two-dimensional finite element model (infinite width assumption (Fig. 3(a))) to determine the limits at which the two-dimensional model breaks down. Here, the thin PDMS layer is modelled as a nearly incompressible nonlinear neo-Hookean elastic beam with Poisson ratio $\nu = 0.495$ and Young's modulus $E = 2$ MPa, based on the nanoidentation tests reported in Appendix B.

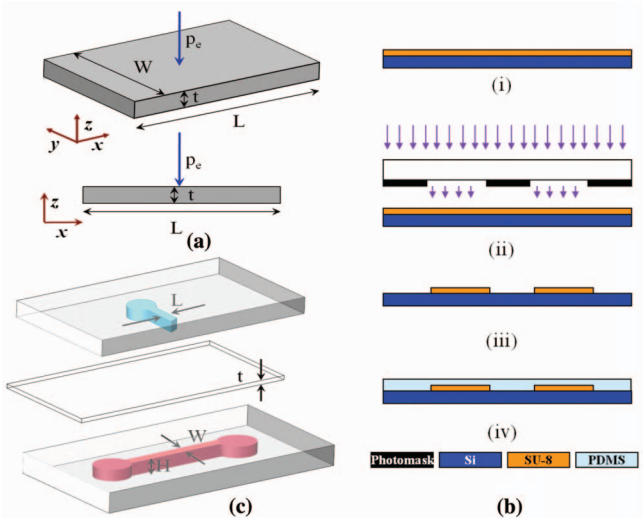

FIG. 3. (a) Illustration of the thin layer geometry indicating the definition of its width and length. (b) Depiction of the main steps involved in the soft lithography procedure used to fabricate the deformable PDMS microchannel: (i) deposition of a SU-8 negative photoresist layer on a silicon wafer via spin coating, (ii) photoresist exposure to UV radiation through a photomask to polymerise the exposed regions, (iii) removal of uncrosslinked photoresist using developer solution to produce the replicated structure on the mould, and (iv) inverse casting of the patterned mould in PDMS upon curing. (c) Exploded view showing the microchannel (maroon) and pressure chamber (cyan) cast separately in two PDMS layers and separated by an additional thin PDMS layer—the area of this layer spanning the microchannel depth W constitutes the thin flexible layer.

III. EXPERIMENTAL DESIGN AND METHODOLOGY

We fabricated the PDMS microfluidic channel depicted in Fig. 3(b) using conventional soft lithography processes involving rapid prototyping and replica moulding.[1,2,38] To prepare the replica moulds, we spin coated multiple layers of SU-8 (SU-8 2035, MicroChem, Newton, MA, USA) negative photoresist onto clean silicon wafers and pre-baked them on a hot plate at 65 °C for 10 min and subsequently 95 °C for 120 min to remove excess photoresist solvent. Repeated layering is required to prepare high aspect ratio moulds possessing final thicknesses of up to 100–200 μm. The photoresist was then exposed to UV radiation at a wavelength of 350–400 nm for 60 s through a quartz photomask on which the device designs shown in Fig. 3(c) were laser printed. This was followed by a two-stage post-exposure bake at 65 °C for 1 min and 95 °C for 20 min to enhance the crosslinking in the exposed portions of the SU-8. Finally, the wafer was developed to remove the photoresist in developer solution for 20 min and the mould dimensions were verified by taking several measurements with a profilometer (Veeco Dektak 150, Plainview, NY; 1 Å maximum vertical resolution).

The base and curing agents of two-part PDMS (Sylgard 184, Dow Corning, Midland, MI, USA) were mixed with a 10:1 ratio and kept in a vacuum chamber to remove any bubbles generated during mixing. The PDMS mixture was then poured over the mould and cured in an oven at 70 °C for 2 h. To ensure that the rigidity of the PDMS was maintained across the devices, the mixing ratio and curing procedure was strictly followed. The PDMS channel replica was then peeled off the mould, and inlet, outlet, and pressure sensor ports were drilled into the structure. Finally, the PDMS channel was oxidised in a plasma cleaner for 2 min and sealed by bonding against a flat PDMS substrate.

The microchannel and pressure chamber are cast in two separate PDMS layers and interleaved with an additional thin PDMS layer for the design shown in Figs. 3(c) and 4. Microchannels with 0.2 $\times$ 10^3, 0.5 $\times$ 10^3, 1.0 $\times$ 10^3, 2.0 $\times$ 10^3, 3.0 $\times$ 10^3, and 4.0 $\times$ 10^3 μm widths were constructed with this technique. The thickness of the flexible thin layer was fabricated to be 60 μm for all channel widths.

A. Deformation of the thin PDMS layer with fluid flow

The deformation of the thin PDMS layer under an external air pressure (Precision pressure regulator IR1020, SMC Pneumatics, Castle Hill, NSW, Australia) applied to the chamber was visually measured using a microscope and video camera (AD3713TB Dino-Lite Premier, AnMo Electronics, Hainchu, Taiwan; 640 $\times$ 480 pixel resolution and 200$\times$ maximum magnification). Nanoindentation experiments, on the other hand, were carried out to evaluate the values of the Young's modulus for the PDMS layers required in the numerical simulations, from which values in the range of 1.2–2.2 MPa were obtained. A detailed description of the nanoindentation test results can be found in Appendix B. Water and sucrose syrup were employed as the working fluid, which were driven through the microchannel at a constant flow rate using a syringe pump connected to the

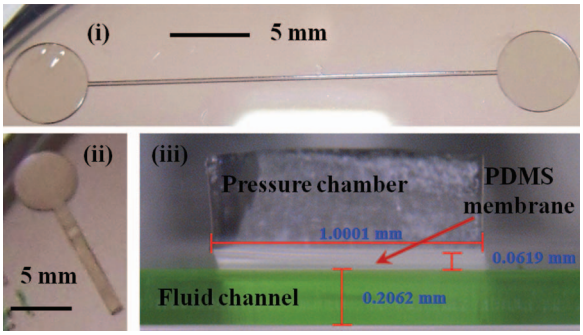

FIG. 4. Images of the patterned SU-8 mould and the PDMS devices for the design depicted in Fig. 3(c). Panel (i) shows the SU-8 mould for the microchannel, panel (ii) shows the pressure chamber mould, and panel (iii) shows a micrograph of the interleaving PDMS layer which constitutes the thin flexible layer separating the microchannel and the pressure chamber.

channel inlet. To measure the pressure drop in the channel, we vertically mount capillary tubes at the inlet and outlet, as illustrated in Fig. 1, and determine the difference in the height across the fluid columns in the capillary tubes.

IV. RESULTS AND DISCUSSION

A. Comparison between the two- and three-dimensional models in the absence of flow

Figure 5(a) depicts the maximum deformation predicted by the two-dimensional and three-dimensional ANSYS simulations (2D/3D-ANSYS) described in Sec. II B, showing that the two-dimensional model begins to deviate from the three-dimensional prediction once the width of the thin layer decreases below $2L$, at which point boundary effects associated with edge pinning on both sides can no longer be neglected. This is consistent with what we observe in the experiments where we measure the deformation of the thin PDMS layer under an external air pressure loading in the absence of fluid flow. Figure 6(a) shows the deformed shape of the thin layer under an externally applied pressure. The maximum deformation of the thin layer, measured at the lowest point of the inflexion of its lower surface, is extracted visually from similar micrographs and shown in Fig. 6(b) as a function of the applied external pressure for microchannels of different widths. The experimental data point presented is the statistical average of at least five values, with vertical bars indicating the range of the deviation; probable sources of the experimental error are the manual handling of the microscope and video camera, visual image analysis to extract the deformed shape of the thin layer, and manual measurement of the fluid column height in the capillary tubes. In agreement with the predictions of the numerical simulations, we see that the deformation becomes independent of the microchannel (and thin layer) width when it exceeds $2L$, therefore suggesting that boundary effects associated with the thin layer pinning at the lateral edges in a three-dimensional model can be neglected and a two-dimensional (infinite width) approximation suffices beyond this critical dimension.

The validity of the two-dimensional incompressible neo-Hookean model (i.e., 2D-FEM-FSI) is further verified against experimental data for microchannels with large widths above $2L$. Figure 5(b) shows a comparison between the maximum deformation measured in the experiments and those predicted by the two-dimensional model, from which we observe agreement with the experimental

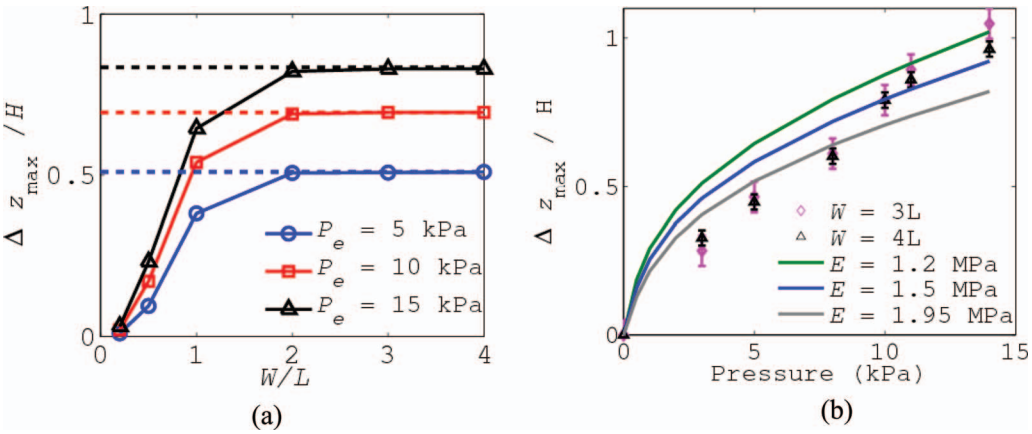

FIG. 5. (a) Maximum deformation of the lower surface of the thin flexible layer Δz_{max} as a function of its width W for three different values of the applied external pressure p_e, as predicted by the 3D-ANSYS simulation described in Sec. II B. The solid lines were added to aid visualisation. Also shown by the dashed lines are the results of a 2D-ANSYS (infinite width assumption) finite element simulation, indicating the diminishing effect of boundary effects associated with the pinned lateral edges in the three-dimensional model above a width of approximately 2×10^3 μm. (b) Comparison of experimental results with the two-dimensional simulation (2D-FEM-FSI), confirming the two-dimensional simulation, beyond a critical width, is an adequate approximation for capturing the deformation behaviour observed in the experiments. Since PDMS has a curing-dependent (and therefore thickness-dependent) Young's modulus, different values of the Young's modulus have been used in the simulations.

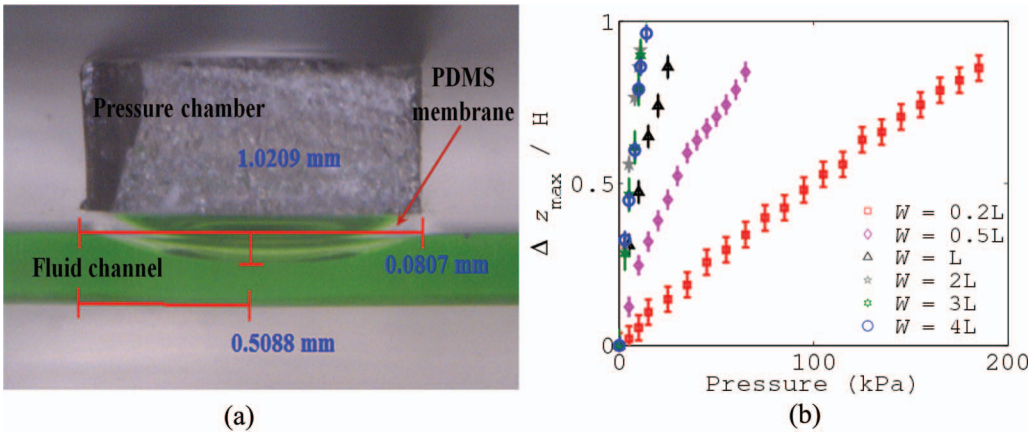

FIG. 6. (a) Micrograph showing the deformation of the thin flexible PDMS layer under the application of an external pressure p_e of 20 kPa for the microchannel designs shown in Fig. 3(b) with a channel width of approximately 0.5×10^3 μm. (b) Maximum deformation of the thin layer Δz_{max}, measured at the lowest point of the inflexion of its lower surface, as a function of the externally applied pressure for microchannels with varying widths.

data to be bounded by the numerical predictions using two values of Young's modulus for the thin layer. We note that the large deformation data are well predicted by a lower value of the Young's modulus whereas better agreement with the small deformation data is captured using a larger value. Both lower and upper values however fall within the 1.2–2.2 MPa range measured using the nanoindentation technique described in Appendix B. In any case, the result provides further evidence to suggest that the two-dimensional model is sufficient to capture the thin layer deformation when it is beyond a critical value of $2L$, which is consistently predicted by both experiment and simulation.

B. Flow experiments: Pressure drop and thin layer deformation

Figure 7 shows the pressure drop Δp as a function of the flow rate Q obtained from both experimental measurements and that predicted by the finite element model (2D-FEM-FSI) described in Sec. II A; the pressure drop measurements were carried out in the absence of an external pressure. Also shown is the pressure drop and flow rate relationship for two-dimensional fully developed viscous flow through a long and rigid rectangular microchannel, for which it is possible to obtain an analytical solution if the channel height H and width W are small compared to the channel length

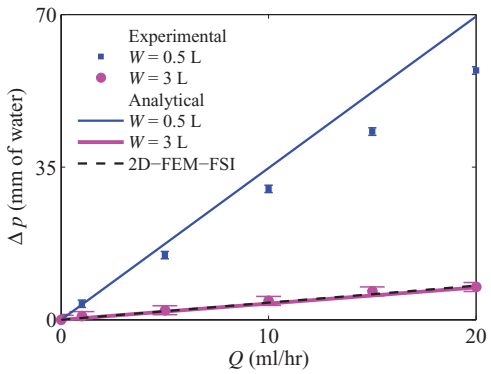

FIG. 7. Relationship between the pressure drop Δp and flow rate Q across a deformable microchannel with two different channel widths. It can be seen that the experimental observations (symbols) match well with the predictions afforded by the finite element simulation (i.e., 2D-FEM-FSI) described in Sec. II A (dashed line) and that for a rigid rectangular microchannel (Eq. (15); solid line). For the narrower channel, however, we observe that the analytical solution for the rigid microchannel overpredicts the pressure drop at higher flow rates. In all of these cases, there is no applied external pressure, i.e. $p_e = 0$.

L—the solution for the longitudinal velocity takes the form[39]

$$v_x = \frac{4H^2\Delta p}{\pi^3\eta L}\sum_{n,odd}^{\infty}\frac{1}{n^3}\left[1-\frac{\cosh(n\pi y/H)}{\cosh(n\pi W/2H)}\right]\sin\left(\frac{n\pi z}{H}\right). \tag{14}$$

Integrating along the width and height of the channel then gives the required pressure drop and flow rate relationship

$$Q = \frac{H^3 W\Delta p}{12\eta L}\left[1-\sum_{n,odd}^{\infty}\frac{192H}{n^5\pi^5 W}\tanh\left(\frac{n\pi W}{2H}\right)\right]. \tag{15}$$

The exact analytical solutions reported in Eqs. (14) and (15) are only valid when the channel is rigid and the cross section of the channel does not vary along its length, when the width of the channel is much greater than its height, and when the Reynolds number is very low ($\mathrm{Re} \lesssim 1$) such that inertial effects can be neglected. The experimental pressure drop and flow rate relationship were in good agreement with those predicted by the analytical solution for a rigid microchannel and the 2D-FEM-FSI for the case of the wide channel. This further suggests that the two-dimensional model constitutes a good approximation when the channel, and hence the thin layer, is sufficiently wide, such that three-dimensional effects (for instance, the pinned boundaries at the sidewalls) can be neglected. The good agreement with the analytical solution, which does not account for the thin flexible layer, also suggests that the effect of the deformation on the pressure drop is small, and hence can be neglected. This is, however, not true for the case of small channel widths in which we observe a departure from the rigid channel prediction at larger flow rates. The cross-sectional area for a $0.5L$ width channel is much lower than that for a $3L$ width channel, and hence the pressure drop is intuitively expected to be higher in the narrower channel for a specified flow rate. However, due to the flexibility of the PDMS channel, we observe some deformation of the channel wall due to the increased fluid stresses at the higher flow rate. This deformation increases the effective cross-sectional area, leading to a reduction in the observed pressure drop. Clearly, the analytical solution for the rigid microchannel cannot account for this deformation, and consequently overpredicts the pressure drop.

Figure 8(a) shows profiles of the deformed thin layer shape under a specified external pressure for varying flow rates (and hence corresponding average inlet velocities U_0), as predicted by the 2D-FEM-FSI simulation described in Sec. II A. We observe no significant deformation of the thin layer below $U_0 = 5 \times 10^{-2}$ m/s corresponding to a flow rate of $Q = 110$ ml/h. This is confirmed in our experiments where we do not observe any measurable changes in the thin layer shape at these

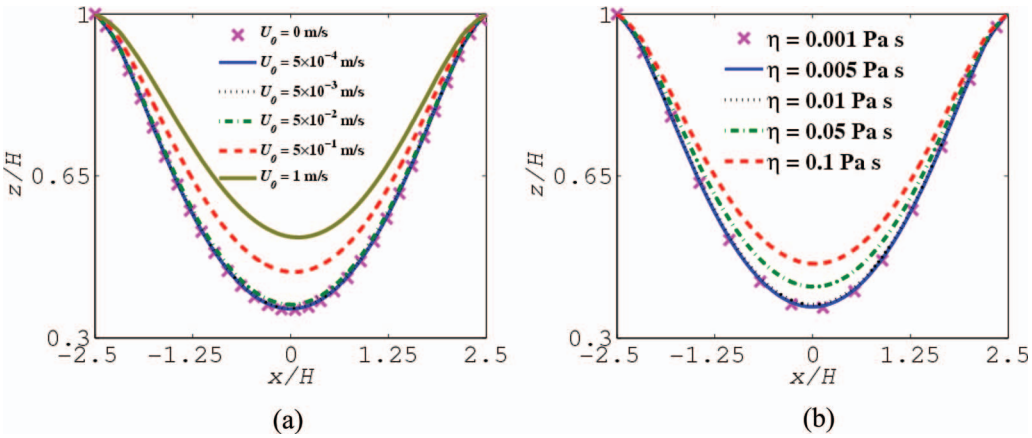

FIG. 8. Shape of the thin layer profile as predicted by the finite element model (i.e., 2D-FEM-FSI) described in Sec. II A for varying (a) average inlet velocity and (b) fluid viscosity. The rest of the parameters used in the simulation are $p_e = 8$ kPa, $E = 1.95$ MPa, $t = 60\,\mu$m, $H = 200\,\mu$m, and $W = 3 \times 10^3\ \mu$m. In (a), the Reynolds number is in the range 0–200 and $\eta = 0.001$ Pa s, whereas in (b), the Reynolds number is in the range 0.01–0.1 with $U_0 = 5 \times 10^{-3}$ m/s.

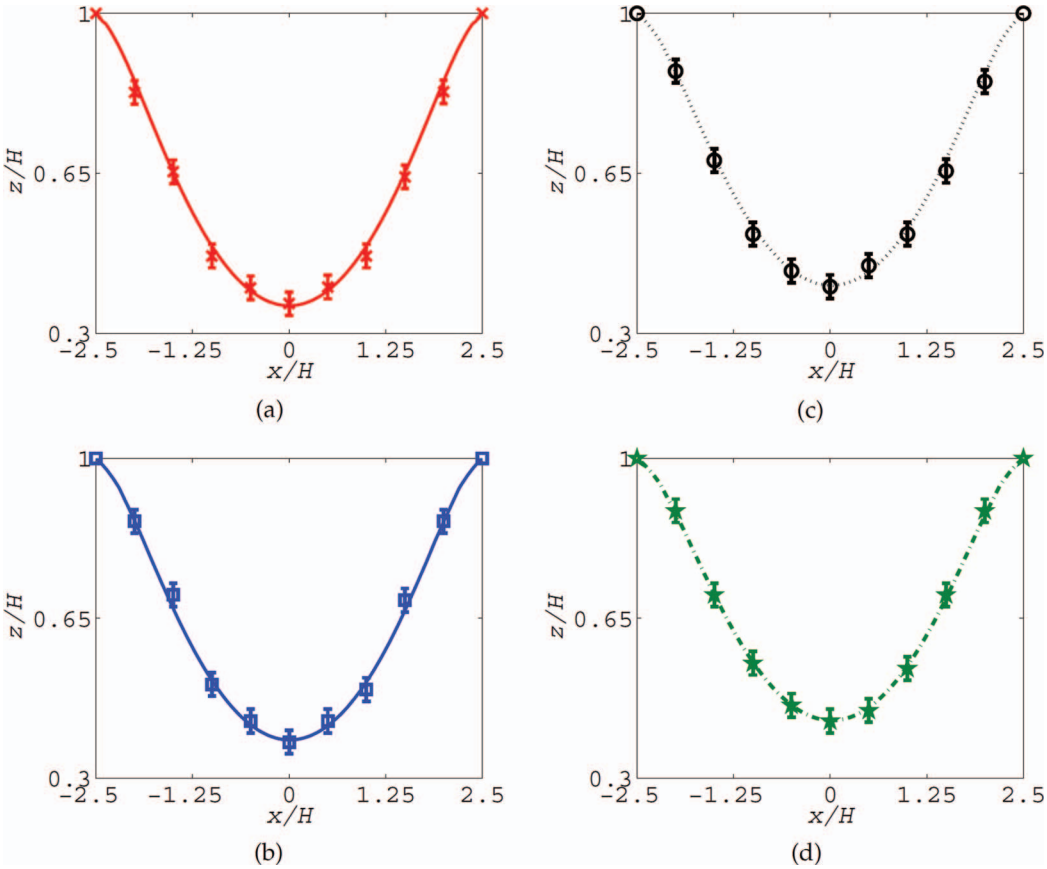

FIG. 9. Comparison of the shape of the thin layer predicted by the 2D-FEM-FSI model (lines) described in Sec. II A with experimental data (symbols) for different inlet fluid velocities: (a) $U_0 = 0$, (b) $U_0 = 2.2 \times 10^{-3}$ m/s, (c) $U_0 = 4.4 \times 10^{-3}$ m/s, and (d) $U_0 = 6.6 \times 10^{-3}$ m/s. The rest of the parameters are $p_e = 8$ kPa, $E = 1.95$ MPa, $t = 60\,\mu$m, $H = 200\,\mu$m, $W = 3 \times 10^3\,\mu$m, and $\eta = 0.05$ Pa s.

flow rates. Restrictions in the maximum flow rate due to experimental limitations, nevertheless, did not allow us to access flow rate regimes where the numerical simulation predicts observable changes in the thin layer shape.

Fortunately, however, the thin layer deformation is sensitive to the fluid viscosity, as shown by the profiles predicted by the numerical simulation in Fig. 8(b). The experiments were therefore repeated under the same conditions but with sucrose syrup with a viscosity of 0.05 Pa s in order to obtain measurable deformations in the thin layer shape. Figure 9 shows close agreement between the experimentally measured and numerically simulated shape of the thin layer profile, the latter (i.e., 2D-FEM-FSI) described in Sec. II A, bolstering confidence in the predictive capability of the proposed model.

V. CONCLUSIONS

To investigate the complex fluid-structural interactions between a microchannel with a deformable wall and the fluid that flows within it, we fabricated a microfluidic device with a single microchannel out of PDMS with a short section comprising a thin flexible layer. Experiments to measure the thin layer deformation and the pressure drop across the channel were complemented by the development and numerical solution of predictive computational models comprising the equations of motion in the fluid coupled with the equilibrium equations governing the elasticity of the thin layer. In particular, we showed that two-dimensional models can only be used to describe a three-dimensional system when the width of the channel, and hence the thin layer, is larger than a

critical dimension, in our case $2L$, such that boundary effects arising from the pinning of the thin layer to the channel walls at its lateral edges can be neglected—a threshold predicted by the simulation that agrees well with our experimental observations. In addition, we find excellent agreement between the predictions of the deformed thin layer shape under an externally applied air pressure using both two-dimensional and three-dimensional models with that measured in the experiments. We believe that the combination of these results, the predictive capability of the numerical models developed, and the physical insight gleaned in this study would be useful in the design of polymer-based microfluidic devices, and in particular, microactuation schemes such as the pneumatically driven micropumps, micromixers, microvalves, and microfilters employing thin flexible polymer layers that have grown increasingly popular over the last decade.

ACKNOWLEDGMENTS

We thank Matteo Pasquali and Marcio Carvalho for providing us with their finite element code for simulating coating flows, which we have modified and adapted to this work. This work was supported by an award under the Merit Allocation Scheme on the NCI National Facility at the Australian National University (ANU). The authors would also like to thank VPAC (Australia) and SUNGRID (Monash University, Australia) for the allocation of computing time on their supercomputing facilities. L.Y. is supported by an Australian Research Fellowship awarded by the Australian Research Council under Discovery Project Grant No. DP0985253. J.R.F. is grateful for the MCN Tech Fellowship from the Melbourne Centre for Nanofabrication and the Vice-Chancellor's Senior Research Fellowship from RMIT University, and acknowledges partial support of this work from the Australian Research Council Grant No. DP120100013 and the use of MCN facilities for fabrication of the structures reported in this study.

APPENDIX A: WEIGHTED RESIDUAL FORM OF THE EQUILIBRIUM EQUATION $\nabla_{\mathbf{X}} \cdot \mathbf{S} = \mathbf{0}$

Here, we provide a correction to the weighted residual form of the equilibrium equation given by Eq. (4) derived by Carvalho and Scriven.[29] The error in the original derivation, while insignificant for small deformations, leads to significant discrepancies when the deformation is large.

The weak form of Eq. (4) is

$$\int_{\overline{\Omega}_S} (\nabla_{\mathbf{X}} \cdot \mathbf{S})\, \phi \; d\overline{\Omega}_S = -\int_{\overline{\Omega}_S} (\nabla_{\mathbf{X}} \phi \cdot \mathbf{S}) \; d\overline{\Omega}_S + \int_{\overline{\Gamma}_S} \phi \, (\mathbf{N} \cdot \mathbf{S}) \; d\overline{\Gamma}_S = \mathbf{0}, \tag{A1}$$

where $\overline{\Omega}_S$, $\overline{\Gamma}_S$, and $\mathbf{N}$ are the area, arc length, and unit normal in the zero-stress configuration, respectively, and ϕ is a weighting function. When written in terms of Cartesian components, the weighted residual form of this equation in the *computational* domain is

$$R_i^x = -\int_{\Omega_{S0}} \left[\frac{\partial \phi_i}{\partial X} S_{Xx} + \frac{\partial \phi_i}{\partial Y} S_{Yx} \right] |\mathbf{J}^*| \, d\Omega_{S0} + \int_{\Gamma_{S0}} \phi_i \, (\mathbf{N} \cdot \mathbf{S})_x \left(\frac{d\overline{\Gamma}_S}{d\Gamma_{S0}} \right) d\Gamma_{S0}, \tag{A2}$$

$$R_i^y = -\int_{\Omega_{S0}} \left[\frac{\partial \phi_i}{\partial X} S_{Xy} + \frac{\partial \phi_i}{\partial Y} S_{Yy} \right] |\mathbf{J}^*| \, d\Omega_{S0} + \int_{\Gamma_{S0}} \phi_i \, (\mathbf{N} \cdot \mathbf{S})_y \left(\frac{d\overline{\Gamma}_S}{d\Gamma_{S0}} \right) d\Gamma_{S0}. \tag{A3}$$

Here, $\overline{\Omega}_{S0}$ and $\overline{\Gamma}_{S0}$ are the area and arc length in the computational domain, respectively, $|\mathbf{J}^*|$ is the Jacobian of the transformation from the zero-stress configuration to the computational domain and ϕ_i is a bi-quadratic weighting function. The components of the dimensional Piola-Kirchhoff stress tensor $\mathbf{S}$, in terms of the *dimensional* Cauchy stress tensor for a neo-Hookean material $\boldsymbol{\sigma} = -\pi^* \mathbf{I} + G\,\mathbf{B}$, are

$$\begin{aligned} S_{Xx} &= -\pi^* \frac{\partial y}{\partial Y} + G \frac{\partial x}{\partial X}, \quad S_{Yx} = \pi^* \frac{\partial y}{\partial X} + G \frac{\partial x}{\partial Y}, \\ S_{Xy} &= \pi^* \frac{\partial x}{\partial Y} + G \frac{\partial y}{\partial X}, \quad S_{Yy} = -\pi^* \frac{\partial x}{\partial X} + G \frac{\partial y}{\partial Y}, \end{aligned} \tag{A4}$$

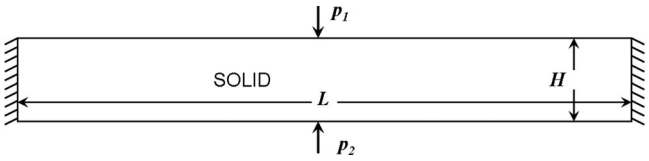

FIG. 10. Geometry of the solid domain of a beam fixed at the edges with uniform pressure applied on both the top and bottom of the beam.

where **I** is the identity tensor, π^* is a pressure-like scalar function and **B** is the left Cauchy-Green tensor. In their finite element formulation of the fluid-structure interaction problem, Carvalho and Scriven[29] (see also Carvalho[40]) have used

$$R_i^x = -\int_{\Omega_{S0}} \left[S_{Xx} \frac{\partial \phi_i}{\partial X} + S_{Xy} \frac{\partial \phi_i}{\partial Y} \right] |\mathbf{J}^*| \, d\Omega_{S0} + \int_{\Gamma_{S0}} \phi_i \, (\mathbf{N} \cdot \mathbf{S})_x \left(\frac{d\overline{\Gamma}_S}{d\Gamma_{S0}} \right) d\Gamma_{S0} \tag{A5}$$

and

$$R_i^y = -\int_{\Omega_{S0}} \left[S_{Yx} \frac{\partial \phi_i}{\partial X} + S_{Yy} \frac{\partial \phi_i}{\partial Y} \right] |\mathbf{J}^*| \, d\Omega_{S0} + \int_{\Gamma_{S0}} \phi_i \, (\mathbf{N} \cdot \mathbf{S})_y \left(\frac{d\overline{\Gamma}_S}{d\Gamma_{S0}} \right) d\Gamma_{S0} \tag{A6}$$

in place of Eqs. (A2) and (A3). Essentially, the positions of the two components S_{Yx} and S_{Xy} have been interchanged.

In order to establish the validity of Eqs. (A2) and (A3) and to demonstrate the incorrectness of Eqs. (A5) and (A6), we have examined the simple problem of a beam fixed at the edges with uniform pressure applied on both the top and bottom of the beam, as shown schematically in Fig. 10. Essentially, we compare the results of our computation using Eqs. (A2) and (A3) (labelled FEM-N), and Eqs. (A5) and (A6) (labelled FEM-C), with the results obtained with the finite element ANSYS simulation for a plane-strain model described in Sec. II B. In addition, we prescribe boundary conditions in the form of zero displacement along the left and right edges of the beam, and a force balance at the top and bottom of the form

$$\mathbf{n} \cdot \boldsymbol{\sigma} = -p_i \, \mathbf{n} \quad (i = 1, 2), \tag{A7}$$

where **n** is the unit normal to the deformed solid surface, and p_1 and p_2 are the dimensional external pressures on the top and bottom of the beam, respectively.

In units of height H, the length of the beam is set at $L = 5H$, with $H = 10^{-3}$ m. The external pressures have been chosen to be $p_1 = 1.1$ N and $p_2 = 1.0$ N, and three different values (6000, 12 000, and 24 000 Pa) have been used for the shear modulus G. Computations have been performed with three different meshes (M1, M2, and M3) in order to examine mesh convergence. We note that the formulation of the fluid-structure interaction problem by Carvalho and Scriven[29] applies to the special case of an *incompressible* neo-Hookean material with a Poisson ratio $\nu = 0.5$. On the other hand, the ANSYS plane-strain package fails for an incompressible neo-Hookean material. Consequently, in order to carry out the comparison with the ANSYS simulations, we have obtained predictions with several values of $\nu < 0.5$, and extrapolated the results to $\nu = 0.5$.

Figure 11 compares the maximum displacement of the beam obtained with the FEM-N and FEM-C formulations with the ANSYS plane-strain model for the three different values of G. In all three cases, mesh-converged results obtained with FEM-N are observed to agree with the extrapolated mesh converged solution obtained with ANSYS. On the other hand, the mesh converged solution obtained with FEM-C shows differences from the other two approaches. Indeed, while this difference is small at $G = 24\,000$ Pa, and substantially larger at $G = 12\,000$ Pa, we are unable to obtain a converged solution with FEM-C at $G = 6000$ Pa.

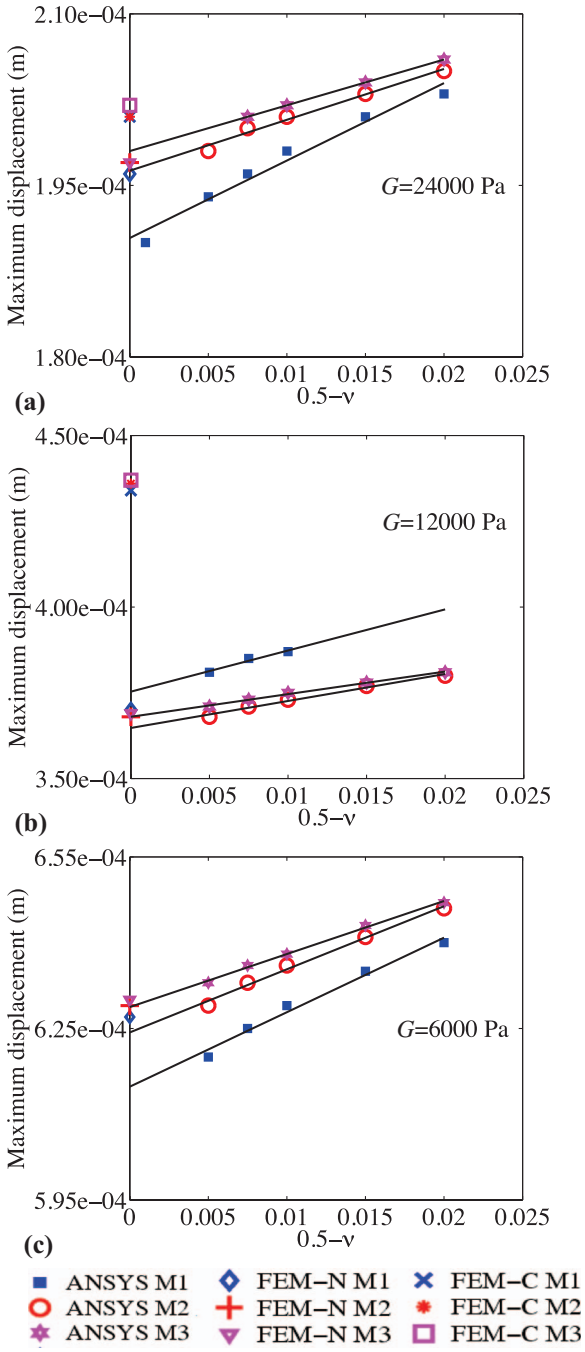

FIG. 11. Comparison between the results for maximum deformation from the FEM-N and FEM-C models with the ANSYS plane-strain model for three different values of G: (a) 24 000 Pa, (b) 12 000 Pa, and (c) 6000 Pa.

APPENDIX B: NANOINDENTATION CHARACTERISATION OF THE ELASTIC MODULUS OF THE THIN PDMS LAYER

Since the Young's modulus of PDMS can be significantly altered by varying the curing temperature and time,[41] and the mixing ratio of the silicone base to the curing agent,[2,8–10] there is a need to measure the isotropic mechanical properties of PDMS.[42–44] Different experimental techniques have been employed to characterise the rigidity of PDMS and the reported value of Young's modulus for PDMS usually falls within the range of 0.05–4.0 MPa.[8,9] Recently, Liu *et al.*[42] have conducted a

tensile test to establish the thickness-dependent hardness and the Young's modulus of thin PDMS layers, arising due to the shear stresses that are exerted during fabrication of these thin layers. On the other hand, nanoindentation testing, which has been widely employed for characterising the elastic and plastic properties of hard materials, is also now being recognised as a tool for characterising the mechanical properties of polymeric materials. In a standard nanoindentation test, the Young's modulus and hardness of a very thin layer made of elastic material can easily be obtained from the load displacement data. Carrillo *et al.*,[45] for example, used a nanoindentation technique to characterise the Young's modulus of PDMS with different degrees of crosslinking.

Here, PDMS (Dow and Corning Sylgard 184) samples were prepared by mixing the cross-linker and siloxane in a ratio of 1:10, and subsequently kept in a vacuum chamber to remove the bubbles that were generated during mixing. Thin PDMS layers with different thicknesses were then produced by spin coating glass wafers at various rotation speeds followed by curing in an oven at 70 °C for 2 h. The thickness of the thin PDMS layer was measured using a surface profiler. By varying the rotation speed of the spin coating process between 500 and 2000 rpm, thin PDMS layers of thicknesses in the range of 25 μm to 100 μm were produced.

The nanoindentation testing is carried out using a TriboIndenter® (Hysitron, Inc., Minneapolis, MN, USA) with a Berkovich indenter tip at room temperature. For load control function, we employ a loading and unloading rate of 10 μN/s, peak load of 100 μN, and a hold period of 5 s. When the tip of the indentor reaches the sample surface, the instrument applies the predefined load and records the load and displacement data accordingly. The hardness and the Young's modulus of the material is then determined from the unloading portion of the load-displacement curve using classical Hertzian contact theory,[46]

$$H = \frac{F_{\max}}{A}, \tag{B1}$$

$$\frac{1}{E_r} = \frac{1-\nu^2}{E} + \frac{1-\nu_i^2}{E_i}, \tag{B2}$$

where H is the hardness of the substrate and $F_{\max}$ is the maximum force applied on the PDMS layer. A is the projected contact area between the tip and the substrate, ν and E are the Poisson's ratio and the Young's modulus for the test specimen, respectively, and ν_i and E_i are those for the indenter. The material properties of the diamond indenter are $E_i = 1140$ GPa and $\nu_i = 0.07$. The reduced elastic modulus E_r is calculated using the following expression proposed by Oliver and Pharr:[47]

$$E_r = \frac{S\sqrt{\pi}}{2\beta\sqrt{A}}, \tag{B3}$$

where S is the contact stiffness, taken as the initial slope of the unloading section of the load-displacement curve, and β is a constant that depends on the geometry of the indenter.

Figure 12(a) shows the indentor displacement in response to the applied load during a nanoindentation test carried out on the thin PDMS layer using quasi-static measurements. To confirm the reproducibility of the test data, the indentation is performed on nine different locations of a given sample. The penetration depth of the indenter is observed to be higher for thinner layers, indicating a lower value for the Young's modulus as the thickness decreases. Similar trends are also observed for other thin PDMS layers.

The reduced elastic modulus E_r and Young's modulus of the thin PDMS layer are calculated using Eqs. (B2) and (B3). Figure 12(b) further indicates that the Young's modulus of the PDMS layers decreases with decreasing thicknesses. This is a consequence of the polymer molecules experiencing enhanced radial stretching due to an increase in the shear stress with the increasing spinning speeds that are required to produce thinner layers. In any case, the good agreement between the measured values for the Young's modulus therefore suggest that the nanoindentation test is capable of differentiating the elastic behaviour of a polymeric material with varying thickness.

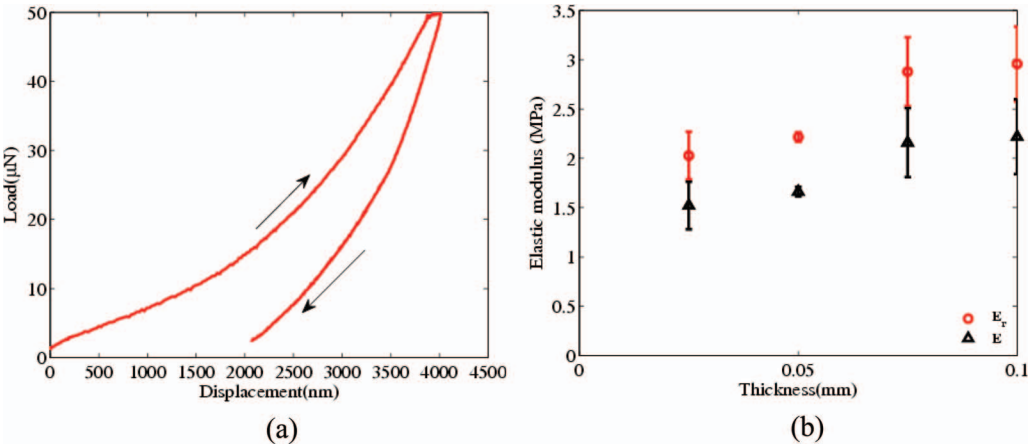

FIG. 12. (a) Load-displacement curves for a thin PDMS layer with a thickness of 0.05 mm. (b) Thickness dependence of the reduced elastic modulus E_r and Young's modulus E of the PDMS layer.

APPENDIX C: VALIDATION OF THE FINITE ELEMENT FORMULATION

Here, we briefly provide results on the validation of the finite element formulation described in Sec. II B against simple benchmark cases that have been reported earlier in the literature.

1. Couette flow past a finite thickness solid

The flow of a Newtonian fluid past an incompressible neo-Hookean solid, as shown schematically in Fig. 13, has been previously described by Gkanis and Kumar.[48] The interface between the fluid and solid is located at $y = t$ and a rigid plate located at $z = (H + t)$ moves in the x direction at a constant speed U_0, giving rise to Couette flow in the fluid domain; the bottom edge of the solid is held fixed. Gkanis and Kumar[48] performed a linear stability analysis of this problem in the limit of zero Reynolds number Re and infinite domain length L, and have shown that the steady-state solution of the deformation in the solid produced by the Couette flow is

$$\boldsymbol{x} = (x, y) = (X + \Gamma Y, Y), \tag{C1}$$

where $\Gamma = (\eta U_0)/(GH)$ is a dimensionless number.

Computations have been performed to compare predictions for the deformation of the solid domain at $L/2$ with the analytical results of Gkanis and Kumar.[48] In order to eliminate end effects caused by the fixed ends of the solid and fluid domains in the computations, we have varied the length of the domain between 10 and 30 m and ensured that domain length independent predictions are obtained. The following parameter values have been used: $\rho = 10^{-3}$ kg/m^3, $\eta = 1$ Pa s, $H = 1$ m, $t = 1$ m, and $U_0 = 1 \times 10^{-3}$–1.75×10^{-3} m/s (such that Re ~ 0) and $G = 10^{-2}$ Pa. The choice of these parameter values maintains Γ in the range 0.1–0.175. The mid-surface displacement of the solid predicted by the finite element formulation is compared with the analytical solution

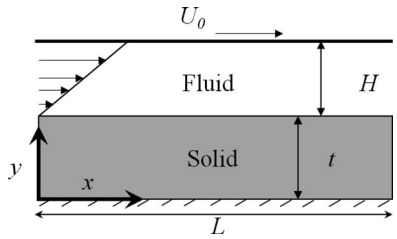

FIG. 13. Schematic depiction of Couette flow of a Newtonian fluid past an incompressible finite thickness neo-Hookean solid.

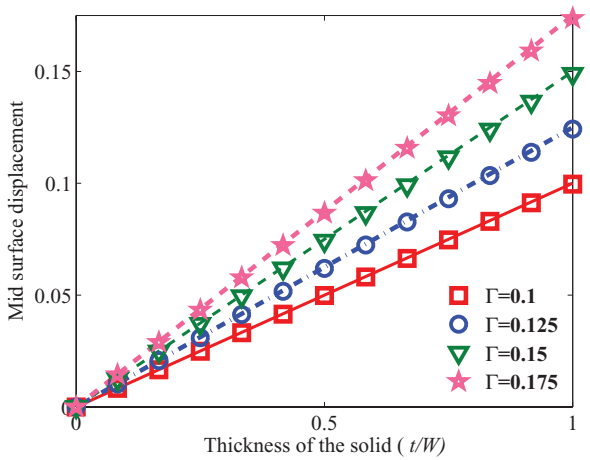

FIG. 14. Comparison of the finite element simulation with the analytical solution for different values of Γ. The lines denote the analytical solution reported by Gkanis and Kumar[48] whereas symbols are the predictions from our simulation.

for different values of Γ. Figure 14 shows that in all cases the predictions of our finite element simulation are in excellent agreement with the analytical solution.

2. Flow in two-dimensional collapsible channels: Elastic beam model

Luo *et al.*[49] have carried out extensive studies of Newtonian fluid flow in a two-dimensional collapsible channel by considering the flexible wall to be a plane-strained elastic beam that obeys Hooke's law. In contrast to the current finite thickness elastic solid model, the beam model does not admit any stress variation across the beam cross section.

For the purposes of comparison, the dimensions of the channel and other parameter values are chosen to be identical to those used by Luo *et al.*[49] in their simulations: $L_u = 5H$, $L = 5H$, $L_d = 30H$, $U_0 = 0.03$ m/s, $H = 10^{-2}$ m, $\rho = 10^3$ kg/m^3, and $\eta = 0.001$ Pa s. The choice of this parameter set corresponds to Re $= 300$. Further, we set $G = 11.97$ kPa (which is equivalent to a value of 35.9 kPa for the Young's modulus of an incompressible solid) and $p_e = 1.755$ Pa. The flexible wall thickness is varied in the range $0.01H$–$0.1H$. We note that the "pre-tension" in the beam is also a variable in the model of Luo *et al.*[49] However, since no such variable exists in the current model, we have restricted our comparison to the results reported by Luo *et al.*[49] for cases where the beam pre-tension is zero.

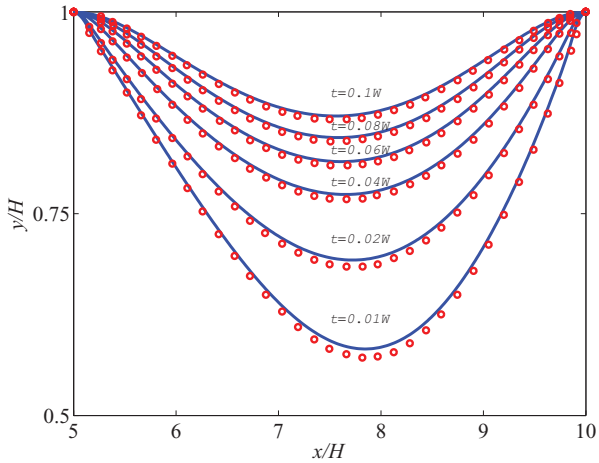

FIG. 15. Comparison of the shape of the flexible wall predicted by the finite thickness elastic solid model with the results of Luo *et al.*[49] for an elastic beam model with different values of the wall thickness. Circles denote the elastic beam model whereas lines denote the results of our numerical simulation.

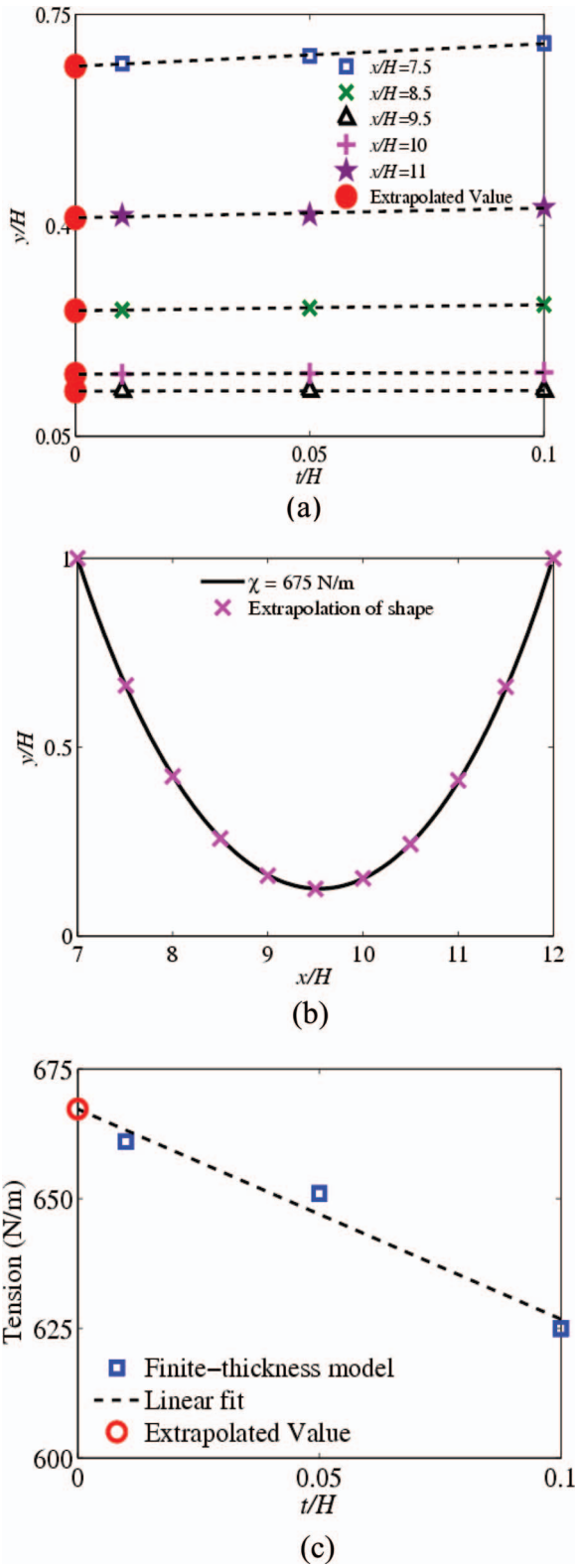

FIG. 16. (a) Extrapolation to $t = 0$ of the flexible wall shape obtained from the finite thickness elastic solid model for $t = 0.01H$, $t = 0.05H$, and $t = 0.1H$. (b) Comparison of the shape of the flexible wall predicted by the finite-thickness solid model (symbols) with the prediction of the zero-thickness thin layer model (solid line). (c) Extrapolation of the average tension acting in the elastic solid to the limit of zero wall thickness.

Figure 15 shows a comparison between the prediction of the shape of the flexible wall of our finite thickness elastic solid model and that reported by Luo *et al.*[49] While our simulations agree with Luo *et al.*[49] for the relatively small deformations that occur at large thin layer thicknesses t, the Hookean beam model, as expected, begins to depart from the prediction of the nonlinear neo-Hookean model for large deformations that are associated with small thin layer thicknesses.

3. Flow in two-dimensional collapsible channels: Zero-thickness thin layer model

Simulations have also been performed to compare predictions of the flexible wall shape from the current finite thickness elastic solid model with the zero-thickness thin layer model of Luo and Pedley[23] for the flow of a Newtonian fluid. Apart from the simplicity of the zero-thickness thin layer model from a constitutive point of view, a fundamental difference between the two models is that while the tension in the flexible wall is prescribed *a priori* in the zero-thickness thin layer model, it is part of the solution in the finite thickness elastic solid model. As a result, a multi-step procedure is required to carry out the comparison, as described in the paragraphs to follow.

The zero-thickness thin layer model is first computed for a pre-determined value of thin layer tension equal to 675 N/m, with the following parameter values: $\mathrm{Re} = 1$, $\rho = 1054\ \mathrm{kg/m^3}$, $U_0 = 1.338 \times 10^{-2}$ m/s, $H = 10^{-2}$ m, $\eta = 0.141$ Pa s, and $p_e = 17\,545\ \mathrm{N/m^2}$. This leads to a prediction of the minimum height of the gap in the channel (beneath the flexible thin layer) of $h/H = 0.125$. Computations with the finite thickness elastic solid model are then carried out for the same parameter values, for various combinations of the flexible wall thickness t and shear modulus G such that each combination always leads to the same value of the minimum channel gap height, namely, $h/H = 0.125$. It turns out that even though the minimum gap height is the same in both models, the predicted interface shape is not, with the difference increasing as the thickness of the elastic solid increases. This is clearly a result of the finite thickness of the elastic solid. Consequently, in order to compare the interface shape, we carry out an extrapolation procedure in which the height of the interface at various locations in the gap as a function of the flexible wall thickness is extrapolated to the limit of zero wall thickness, as shown in Fig. 16(a). The extrapolated interface shape is then compared with the prediction by the zero-thickness thin layer model in Fig. 16(b), in which we observe excellent agreement between the two models.

The remaining step involves the evaluation of the resultant tension in the finite thickness elastic solid and how it compares with the pre-determined thin layer tension of 675 N/m. Here, we first estimate the tension in the finite thickness solid at a particular location x by averaging the tangential solid stresses acting across the cross section at x. An estimate of the overall tension in the solid is then obtained by averaging the tension along the entire length of the flexible solid for all values of x. The values of the average tension obtained from the finite thickness elastic solid model for $t = 0.01H$, $t = 0.05H$, and $t = 0.1H$ are then extrapolated to $t = 0$, as shown in Fig. 16(c), in which we observe the extrapolated value of tension to be fairly close to the value of 675 N/m used in the zero-thickness thin layer model.

[1] J. M. K. Ng, I. Gitlin, A. D. Stroock, and G. M. Whitesides, "Components for integrated poly(dimethylsiloxane) microfluidic systems," Electrophoresis **23**, 3461–3473 (2002).
[2] J. Friend and L. Yeo, "Fabrication of microfluidic devices using polydimethylsiloxane," Biomicrofluidics **4**, 026502 (2010).
[3] L. Y. Yeo, H.-C. Chang, P. P. Y. Chan, and J. R. Friend, "Microfluidic devices for bioapplications," Small **7**, 12–48 (2011).
[4] T. Vestad, D. W. M. Marr, and J. Oakey, "Flow control for capillary-pumped microfluidic systems," J. Micromech. Microeng. **14**, 1503–1506 (2004).
[5] C. H. Wang and G. B. Lee, "Pneumatically driven peristaltic micropumps utilizing serpentine-shape channels," J. Micromech. Microeng. **16**, 341–348 (2006).
[6] D. Irimia and M. Toner, "Cell handling using microstructured membranes," Lab Chip **6**, 345–352 (2006).
[7] S.-B. Huang, M.-H. Wu, and G.-B. Lee, "A tunable micro filter modulated by pneumatic pressure for cell separation," Sens. Actuators B **142**, 389–399 (2009).
[8] A. L. Thangawng, R. S. Ruoff, M. A. Swartz, and M. R. Glucksberg, "An ultra-thin PDMS membrane as a bio/micronano interface: Fabrication and characterization," Biomed. Microdevices **9**, 587–595 (2007).
[9] D. Fuard, T. Tzvetkova-Chevolleau, P. T. S. Decossas, and P. Schiavone, "Optimization of poly-di-methyl-siloxane (PDMS) substrates for studying cellular adhesion and motility," Microelectron. Eng. **85**, 1289–1293 (2008).
[10] D. N. Hohne, J. G. Younger, and M. J. Solomon, "Flexible microfluidic device for mechanical property characterization of soft viscoelastic solids such as bacterial biofilms," Langmuir **25**, 7743–7751 (2009).

[11] M. A. Unger, H. P. Chou, T. Thorsen, A. Scherer, and S. R. Quake, "Monolithic microfabricated valves and pumps by multilayer soft lithography," Science **288**, 113–116 (2000).
[12] D. Irimia, S.-Y. Liu, W. Tharp, A. Samadani, M. Toner, and M. Poznansky, "Microfluidic system for measuring neutrophil migratory responses to fast switches of chemical gradients," Lab Chip **6**, 191–198 (2006).
[13] W. A. Conrad, "Pressure-flow relationships in collapsible tubes," IEEE Trans. Bio-Med. Eng. **16**, 284–295 (1969).
[14] R. W. Brower and C. Scholten, "Experimental evidence on the mechanism for the instability of flow in collapsible vessels," Med. Biol. Eng. **13**, 839–844 (1975).
[15] C. D. Bertram, "Two modes of instability in a thick-walled collapsible tube conveying a flow," J. Biomech. **15**, 223–224 (1982).
[16] C. D. Bertram, "Unstable equilibrium behaviour in collapsible tubes," J. Biomech. **19**, 61–69 (1986).
[17] C. D. Bertram, "The effects of wall thickness, axial strain and end proximity on the pressure-area relation of collapsible tubes," J. Biomech. **20**, 863–876 (1987).
[18] C. D. Bertram, C. J. Raymond, and T. J. Pedley, "Mapping of instabilities during flow through collapsed tubes of differing length," J. Fluids. Struct. **4**, 125–153 (1990).
[19] C. D. Bertram, C. J. Raymond, and T. J. Pedley, "Application of non-linear dynamics concepts to the analysis of self-excited oscillations of a collapsible tube conveying a flow," J. Fluids. Struct. **5**, 391–426 (1991).
[20] C. D. Bertram and S. A. Godbole, "LDA measurements of velocities in a simulated collapsed tube," ASME J. Biomech. Eng. **119**, 357–363 (1997).
[21] C. D. Bertram and R. Castles, "Flow limitation in uniform thick-walled collapsible tubes," J. Fluids Struct. **13**, 399–418 (1999).
[22] C. D. Bertram and N. S. J. Elliott, "Flow-rate limitation in a uniform thin-walled collapsible tube, with comparison to a uniform thick-walled tube and a tube of tapering thickness," J. Fluids Struct. **17**(4), 541–559 (2003).
[23] X. Y. Luo and T. J. Pedley, "A numerical simulation of steady flow in a 2-D collapsible channel," J. Fluids Struct. **9**, 149–174 (1995).
[24] X. Y. Luo and T. J. Pedley, "A numerical simulation of unsteady flow in a two-dimensional collapsible channel," J. Fluid Mech. **314**, 191–225 (1996).
[25] A. L. Hazel and M. Heil, "Steady finite-Reynolds-number flows in three-dimensional collapsible tubes," J. Fluid Mech. **486**, 79–103 (2003).
[26] M. Heil and O. E. Jensen, "Flows in deformable tubes and channels—Theoretical models and biological applications," in *Flow Past Highly Compliant Boundaries and in Collapsible Tubes*, edited by P. W. Carpenter and T. J. Pedley (Kluwer, Dordrecht, 2003), pp. 15–50.
[27] A. Marzo, X. Luo, and C. Bertram, "Three-dimensional collapse and steady flow in thick-walled flexible tubes," J. Fluids. Struct. **20**, 817–835 (2005).
[28] H. F. Liu, X. Y. Luo, Z. X. Cai, and T. J. Pedley, "Sensitivity of unsteady collapsible channel flows to modelling assumptions," Commun. Numer. Methods Eng. **25**, 483–504 (2009).
[29] M. S. Carvalho and L. E. Scriven, "Flows in forward deformable roll coating gaps: Comparison between spring and plane strain models of roll cover" J. Comput. Phys. **138**, 449–479 (1997).
[30] J. M. deSantos, "Two-phase cocurrent downflow through constricted passages," Ph.D. dissertation (University of Minnesota, Minneapolis, MN, 1991).
[31] K. N. Christodoulou and L. E. Scriven, "Discretization of free surface flows and other moving boundary problems," J. Comput. Phys. **99**, 39–55 (1992).
[32] D. F. Benjamin, "Roll coating flows and multiple roll systems," Ph.D. dissertation (University of Minnesota, Minneapolis, MN, 1994).
[33] M. Pasquali and L. E. Scriven, "Free surface flows of polymer solutions with models based on the conformation tensor," J. Non-Newtonian Fluid Mech. **108**, 363–409 (2002).
[34] G. A. Zevallos, M. S. Carvalho, and M. Pasquali, "Forward roll coating flows of viscoelastic liquids," J. Non-Newtonian Fluid Mech. **130**, 96–109 (2005).
[35] M. Bajaj, J. R. Prakash, and M. Pasquali, "A computational study of the effect of viscoelasticity on slot coating flow of dilute polymer solutions," J. Non-Newtonian Fluid Mech. **149**, 104–123 (2008).
[36] D. Chakraborty, M. Bajaj, L. Yeo, J. Friend, M. Pasquali, and J. R. Prakash, "Viscoelastic flow in a two-dimensional collapsible channel," J. Non-Newtonian Fluid Mech. **165**, 1204–1218 (2010).
[37] ANSYS, Structural analyses guide, Mechanical APDL, Release 11.0, ANSYS, Inc., Canonsburg, PA, USA, 2010.
[38] D. C. Duffy, J. C. McDonald, O. J. A. Schueller, and G. M. Whitesides, "Rapid prototyping of microfluidic systems in poly (dimethylsiloxane)," Anal. Chem **70**, 4974–4984 (1998).
[39] N. Mortensen, F. Okkels, and H. Bruus, "Reexamination of Hagen-Poiseuille flow: Shape dependence of the hydraulic resistance in microchannels," Phys. Rev. E **71**, 057301 (2005).
[40] M. S. Carvalho, "Roll coating flows in rigid and deformable gaps," Ph.D. dissertation (University of Minnesota, Minneapolis, MN, 1996).
[41] H. Schmid and B. Michel, "Siloxane polymers for high-resolution, high-accuracy soft lithography," Macromolecules **33**, 3042–3049 (2000).
[42] M. Liu, J. Sun, Y. Sun, C. Bock, and Q. Chen, "Thickness-dependent mechanical properties of polydimethylsiloxane membranes," J. Micromech. Microeng. **19**, 035028 (2009).
[43] M. Liu, J. Sun, and Q. Chen, "Influences of heating temperature on mechanical properties of polydimethylsiloxane," Sens. Actuators A **151**, 42–45 (2009).
[44] T. Kim, J. Kim, and O. Jeong, "Measurement of nonlinear mechanical properties of PDMS elastomer," Microelectron. Eng. **88**, 1982–1985 (2011).

[45] F. Carrillo, S. Gupta, M. Balooch, S. J. Marshall, G. W. Marshall, L. Pruitt, and C. Puttlitz, "Nanoindentation of polydimethylsiloxane elastomers: Effect of crosslinking, work of adhesion, and fluid environment on elastic modulus," J. Mater. Res. **20**, 2820–2830 (2005).
[46] K. Johnson, *Contact Mechanics* (Cambridge University Press, Cambridge, 2003).
[47] W. C. Oliver and G. M. Pharr, "An improved technique for determining hardness and elastic modulus using load and displacement sensing indentation experiments," J. Mater. Res. **7**, 1564–1583 (1992).
[48] V. Gkanis and S. Kumar, "Instability of creeping Couette flow past a neo-Hookean solid," Phys. Fluids **15**, 2864–2871 (2003).
[49] X. Y. Luo, B. Calderhead, H. F. Liu, and W. G. Li, "On the initial configurations of collapsible tube flow," Comput. Struct. **85**, 977–987 (2007).